Force chains and contact network topology in sheared packings of elongated particles

Emilien Azéma* and Farhang Radjai†

LMGC, Université Montpellier 2, CNRS, Place Eugène Bataillon, 34095 Montpellier cedex 05, France

(Received 1 August 2011; revised manuscript received 12 January 2012; published 19 March 2012)

By means of contact dynamic simulations, we investigate the contact network topology and force chains in two-dimensional packings of elongated particles subjected to biaxial shearing. The morphology of large packings of elongated particles in quasistatic equilibrium is complex due to the combined effects of local nematic ordering of the particles and orientations of contacts between particles. The effect of elongation on shear behavior and dilatancy was investigated in detail in a previous paper [Azéma and Radjai, Phys. Rev. E **81**, 051304 (2010)]. Here, we show how particle elongation affects force distributions and force-fabric anisotropy via various local structures allowed by steric exclusions and the requirement of force balance. We find that the force distributions become increasingly broader as particles become more elongated. Interestingly, the weak force network transforms from a passive stabilizing agent with respect to strong force chains to an active force-transmitting network for the whole system. The strongest force chains are carried by side-side contacts oriented along the principal stress direction.

DOI: 10.1103/PhysRevE.85.031303 PACS number(s): 45.70.−n, 83.80.Fg, 61.43.−j

I. INTRODUCTION

Most remarkable properties of granular materials are closely related to their specific disorder induced essentially by steric exclusions and the force balance condition for each particle. The broad and strongly inhomogeneous distribution of contact forces, as a hallmark of granular disorder, has been a subject of extensive investigation [1–10]. In spite of particle mobility and disorder, granular materials exhibit a finite shear strength due to a genuine anisotropic two-phase organization of the contact network involving strong force chains propped by weak forces [11].

The robustness of these microstructural features with respect to particle geometry and interactions has been addressed only recently by discrete-element numerical simulations. For example, it is found that in highly polydisperse systems the force chains are mainly captured by large particles so that the shear strength of a noncohesive granular material is practically independent of particle-size distribution [12]. As another important example, a parametric study shows that when the particles interact by both sliding friction and high rolling resistance at their contacts, the nature of the weak network is affected by the formation of columnar structures, which do not need to be propped by a particular class of weak contacts [13].

The particle shape is another major characteristic of granular material. Most applications of real granular materials involve some degree of deviation with respect to simple circular or spherical shapes often used in simulations by the discrete-element method. While the numerical treatment of large packings of complex particle shapes was until very recently out of reach due to demanding computational resources, there is presently considerable scope for the numerical investigation of complex granular packings. This is not only due to the enhanced computer power and memory but also because during more than two decades of research in this field, many properties of granular media have been investigated for model packings composed of circular and spherical particle shapes. Such properties thus provide a rich guideline for the analysis of specific behaviors arising from particle geometry.

Systematic studies of particle shape dependence in granular materials have been recently reported for polygonal and polyhedral [14–17], elliptical and ellipsoidal [18–21], and nonconvex shapes [22]. The force chains are found to be reinforced in packings of polygonal and polyhedral particles, leading to enhanced shear strength [15,18,23]. The effect of shape elongation was investigated for packings of rectangular-shaped particles deposited under gravity [24,25]. The preparation under gravity has strong influence on the particle orientations and thus on the force distributions. On the other hand, a systematic study of the shear behavior of two-dimensional (2D) packings of rounded-cap rectangles (RCR) under homogeneous boundary conditions indicates that the shear strength increases with elongation whereas the packing fraction varies unmonotonically [18], as also found for packings of ellipsoidal shapes [20,21].

In all reported cases, the networks resulting from various shapes appear to be highly complex and hardly amenable to simple statistical modeling. In this paper, we investigate the contact and force networks in sheared granular packings of elongated particles in two dimensions with increasing aspect ratio. The numerical samples are composed of RCR particles and basically identical to those used for the investigation of the effect of particle elongation on the shear and volume-change behavior in a previous paper [18]. In this work, we focus more specifically on the organization of the contact force network in correlation with the fabric anisotropy described in terms of branch vectors joining particle centers. Our data reveal a bimodal force network as in disk packings but with qualitatively different roles of fabric and force anisotropies. This behavior involves a short-range nematic ordering of the particles with side-side contacts that capture stronger force chains. On the other hand, the friction mobilization is shown to be anisotropic and it plays a major role in the stability of elongated particles.

*emilien.azema@univ-montp2.fr
†franck.radjai@univ-montp2.fr

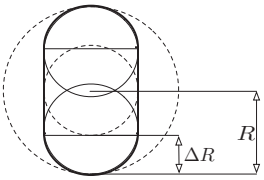

FIG. 1. Shape of a rounded-cap rectangle (RCR).

In the following, we first summarize our numerical procedures as described in more detail in Ref. [18]. Some salient results of that work will be recalled, too. Then, we analyze the microstructure of the samples in terms of the branch vectors and their correlations with the contact forces. Finally, we present a detailed analysis of the partial stresses and fabric anisotropies sustained by force subnetworks. We conclude with a summary of the main results of this work and its possible applications.

II. BRIEF DESCRIPTION OF NUMERICAL PROCEDURES AND PREVIOUS WORK

The simulations were carried out by means of the contact dynamics (CD) method as a discrete element model (DEM) of rigid particles [10,26–35]. As described in more detail in Ref. [18], we model the RCR particle as a juxtaposition of two half-disks of radius R' with one rectangle of length L and width $2R'$ as shown in Fig. 1. The shape of a RCR particle is a circle of radius R' for $L = 0$. To represent the deviation of the particle shape from a circle, we define the dimensionless parameter η given by

$$\eta = \frac{\Delta R}{R}, \tag{1}$$

where $R = L/2 + R'$ is the radius of the circle circumscribing the particle and $\Delta R = R - R' = L/2$. η varies from 0 for a circle to 1 for a line.

Eight different packings of 13 000 RCR particles are prepared with η varying from 0 to 0.7 by steps of 0.1. The radius R of the circumscribing circle defines the size of a RCR particle. A size polydispersity is also introduced by taking R in the range $[R_{\min}, R_{\max}]$ with $R_{\max} = 2R_{\min}$ with a uniform distribution in particle volume fractions. The samples are prepared by random sequential deposition in a rectangular box [36–38], followed by isotropic compaction. Figure 2 displays snapshots of the packings for several values of η at the end of isotropic compaction. The isotropic samples are then sheared by applying a low velocity on the top wall at constant velocity for a constant confining stress acting on the lateral walls.[1] The friction coefficient μ between particles is set to 0.5 and to 0 with the walls. The shear is essentially quasistatic so that the kinetic energy is negligible compared to the applied lateral stress.

In Ref. [18], the stress-strain behavior was studied in detail as a function of particle elongation. The stress tensor $\boldsymbol{\sigma}$ in the volume V is an arithmetic mean involving the branch vectors $\boldsymbol{\ell}^c$

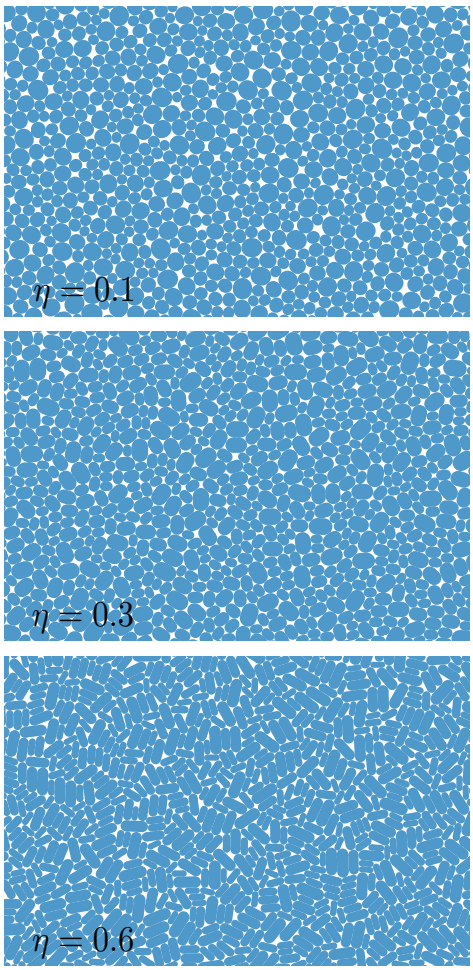

FIG. 2. (Color online) Examples of the generated packings at the initial state.

(joining the centers of the two touching particles) and contact force vectors $\boldsymbol{f}^c$ at contact c, and it is given by [39,40]

$$\boldsymbol{\sigma} = \frac{1}{V} \sum_{c \in V} f^c_\alpha \ell^c_\beta. \tag{2}$$

Hence, the internal angle of friction φ of a granular sample in the course of its evolution is given by

$$\sin\varphi = \frac{q}{p} = \frac{\sigma_1 - \sigma_2}{\sigma_1 + \sigma_2}, \tag{3}$$

where σ_1 and σ_2 are the principal stresses. Starting with an initially dense state, the shear stress tends to a nearly constant value corresponding to the critical state, which is independent of the initial packing configuration. In parallel, all packings, which are prepared initially by isotropic compaction in a dense state, dilate monotonically and tend to a constant packing fraction in the critical state.

It was shown in Ref. [18] that $\sin\varphi$, evaluated in the critical state for different samples, increases linearly with η. The "microscopic" origin of this behavior was analyzed by means of an additive decomposition of the stress tensor. It was shown that the increasing mobilization of friction force and the associated anisotropy are the key effects of particle shape elongation. In the critical state, the proportion of sliding

[1] See [http://cgp-gateway.org/ref010 for video samples].

contacts increases with η in correlation with a local nematic ordering of the particles tending to be oriented perpendicular to the major principal stress direction. Another interesting finding was the rather counterintuitive result that the packing fraction first increases with particle elongation but then declines to lower values for more elongated particles. Remarkably, the coordination number does not follow this trend but increases with elongation, so that the packings of the most elongated particles are loose but well connected.

In this paper, the simulation data are exploited in order to characterize more specifically the effect of shape elongation with respect to the contact network and force transmission in the critical state. We present a detailed description of the distributions of branch vectors, contact forces, and friction mobilization. Then, we focus on the weak and strong force networks and their properties as functions of elongation.

III. DISTRIBUTIONS OF CONTACT FORCES AND BRANCH VECTORS

A common approach used by various authors is to express branch vectors and contact force orientations in terms of the contact direction, that is, in the local *contact frame* $(\boldsymbol{n},\boldsymbol{t})$, where $\boldsymbol{n}$ is the unit vector perpendicular to the contact plane and $\boldsymbol{t}$ is the orthonormal counterclockwise unit vector as shown in Fig. 3. The components of the branch vector and contact force are expressed in the following frame:

$$\begin{aligned} \boldsymbol{\ell} &= \ell_n \boldsymbol{n} + \ell_t \boldsymbol{t}, \\ \boldsymbol{f} &= f_n \boldsymbol{n} + f_t \boldsymbol{t}, \end{aligned} \tag{4}$$

where ℓ_n and ℓ_t are the normal and tangential components of the branch vectors, and f_n and f_t the normal and tangential components of the contact force. Note that only for disks or spherical particles do we have $\boldsymbol{\ell} = \ell \boldsymbol{n}$, where ℓ is the length of the branch vector.

A specific feature of the contact network of a packing of elongated particles is that the length ℓ of branch vectors strongly varies throughout the network depending on the relative particle orientations. From the definition of η [Eq. (1)] and for given values of $R_{\min}$ and $R_{\max}$, it is easy to see that

$$\frac{\ell}{R_{\max}} \in \left[2\frac{R_{\min}}{R_{\max}}(1-\eta), 2 \right]. \tag{5}$$

In our simulations, since $R_{\min}/R_{\max} = 0.5$, we have $(1-\eta)R_{\max} \leqslant \ell \leqslant 2R_{\max}$. With increasing elongation η, the range of ℓ becomes significant and its statistics can be used as a meaningful characterization of the texture as a function of η. On the other hand, the correlation of ℓ with the total reaction force f between neighboring particles seems to be a good descriptor of the organization of forces for particles of noncircular shape. The branch vectors are also important as they enter the expression of the stress tensor given by Eq. (2). In Ref. [18], a different point of view was adopted: The contact forces were projected along and perpendicular to the branch vectors and their statistics were investigated. The same framework was used for the decomposition of the total stress tensor. Here, we focus on the distribution of contact forces and their correlation with the branch vector as η is increased.

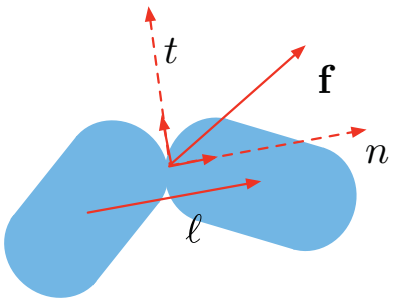

FIG. 3. (Color online) Local contact frame $(\boldsymbol{n},\boldsymbol{t})$.

A. Contact forces and friction mobilization

The probability density function (PDF) of normal forces normalized by the mean normal force $\langle f_n \rangle$ is shown in Fig. 4 in log-linear and log-log scales at large strains (the data are cumulated from several snapshots in the critical state) for all simulated values of η. As usually observed, in all packings the number of forces above the mean $\langle f_n \rangle$ falls off exponentially whereas the number of forces below the mean varies as a power law:

$$P(f_n) \propto \begin{cases} e^{-\alpha_n(\eta)(f_n/\langle f_n \rangle)}, & f_n > \langle f_n \rangle, \\ \left(\frac{f_n}{\langle f_n \rangle}\right)^{\beta_n(\eta)}, & f_n < \langle f_n \rangle, \end{cases} \tag{6}$$

where $\alpha_n(\eta)$ and $\beta_n(\eta)$, whose variations are shown in the insets, are functions of η. We see that α_n decreases with increasing η, implying that the inhomogeneity of normal forces becomes higher as the particles become more elongated. On the other hand, β_n declines from 0.1 to -0.4 with η, which means

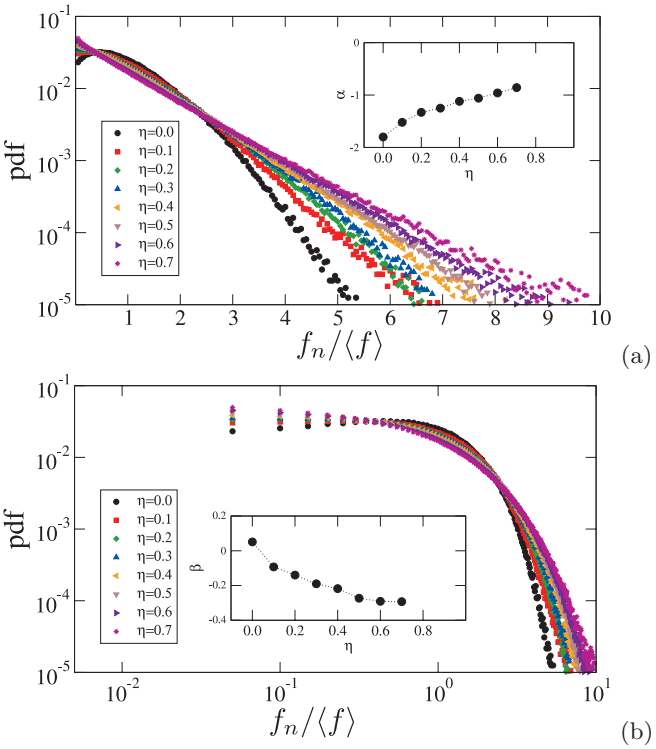

FIG. 4. (Color online) Probability distribution function of normal forces f_n normalized by the average normal force $\langle f_n \rangle$ in log-linear (a) and log-log (b) scales for different values of η.

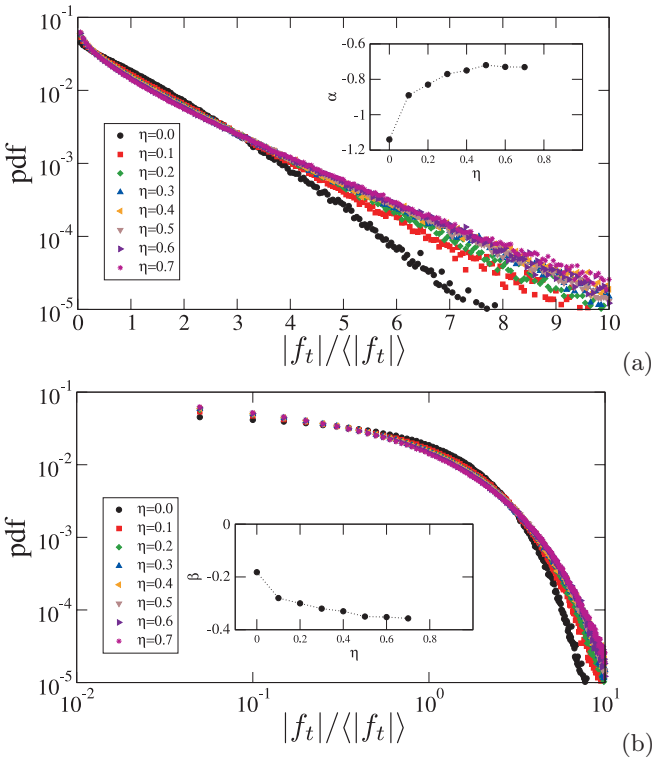

FIG. 5. (Color online) Probability distribution function of tangential forces f_t normalized by the average tangential force $\langle f_t \rangle$ in log-linear (a) and log-log (b) scales for different values of η.

that the proportion of weak contacts (carrying a normal force below the mean) increases with elongation. The proportion of weak forces grows from 60% for $\eta = 0$ to 70% for $\eta = 0.7$. In other words, while the proportion of strong contacts declines with increasing η, stronger force chains occur at the same time.

Figure 5 shows the PDF $P(f_t)$ of tangential forces normalized by the mean tangential force $\langle|f_t|\rangle$ in each packing. These distributions show also an exponential falloff for the forces above the average force $\langle|f_t|\rangle$ and a power law for the forces below $\langle|f_t|\rangle$:

$$P(f_t) \propto \begin{cases} e^{-\alpha_t(\eta)(|f_t|/\langle|f_t|\rangle)}, & |f_t| > \langle|f_t|\rangle, \\ \left(\frac{|f_t|}{\langle|f_t|\rangle}\right)^{\beta_t(\eta)}, & |f_t| < \langle|f_t|\rangle, \end{cases} \tag{7}$$

the corresponding exponents $\alpha_t(\eta)$ and $\beta_t(\eta)$ decreasing with η. We observe that, in contrast to α_n and β_n, the exponents α_t and β_t saturate beyond $\eta = 0.4$. This means that the friction forces do not follow the normal forces as η increases. In other words, the most mobilized (largest) friction forces do not occur necessarily at the contacts where the normal forces are higher.

In order to investigate the properties of friction mobilization, we consider the friction mobilization index $I_m = |f_t|/\mu f_n$. Its average $I_M = \langle \frac{|f_t|}{\mu f_n} \rangle$ increases from 0.4 for $\eta = 0$ to 0.6 for $\eta = 0.7$ as we see in Fig. 6. This increase underlies to a large extent the increase of the shear strength with η, as we see in Sec. IV. However, the friction force is not uniformly mobilized at all contacts. Figure 7 shows a map of weak ($f_n < \langle f_n \rangle$) and strong ($f_n > \langle f_n \rangle$) normal forces, represented by the thickness of vectors joining the particle

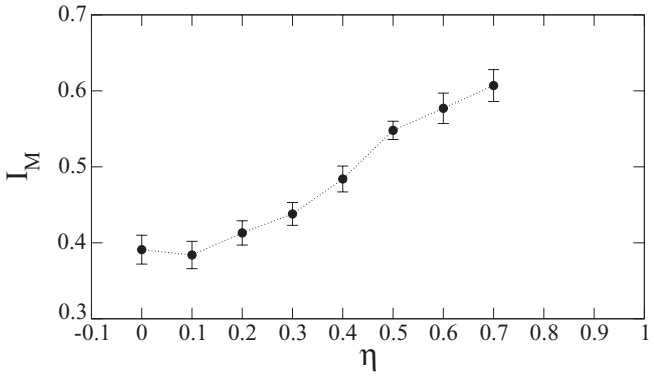

FIG. 6. Friction mobilization I_M averaged in the critical state as function of η.

centers to the contact points, and the corresponding values of I_m, represented by circles with diameters proportional to I_m for $\eta = 0.1$ and $\eta = 0.7$. Visual inspection reveals that most mobilized contacts belong to the weak force network. In fact, the average friction mobilization I_{mf} defined as the average by force class, plotted as a function of f_n in Fig. 8 for all values of η, declines as f_n increases. We also see that the friction mobilization increases with η at all force levels.

Figure 9 displays the pdf of I_m for different values of η in the critical state. For the disks, the PDF is a nearly decreasing linear function of I_m, which means that the proportion of weakly mobilized contacts is larger than that of strongly

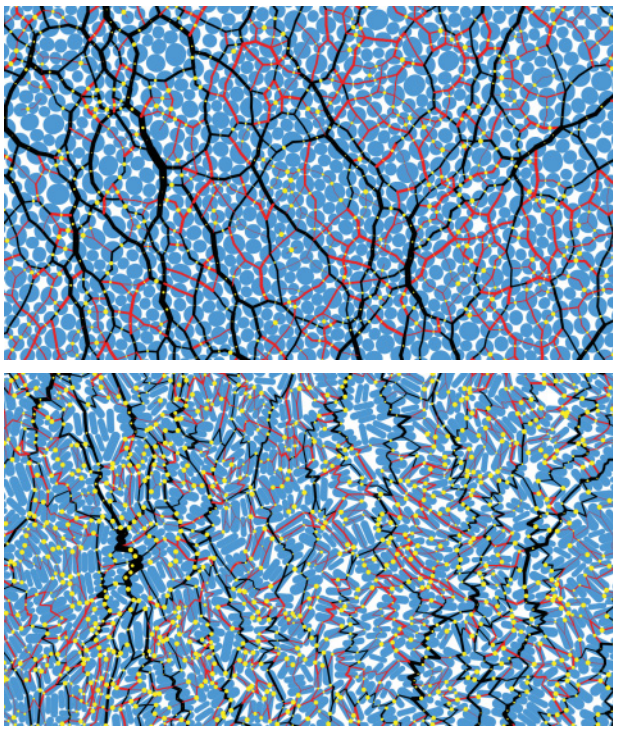

FIG. 7. (Color online) A snapshot of the force-bearing particles at $\eta = 0.2$ (a) and $\eta = 0.7$ (b) and normal forces represented by the thickness of the segments joining the particle centers to the application point of the force. The strong and weak forces are in black and red (dark gray), respectively. The diameter of the yellow (light gray) circle is proportional to I_m at the contact.

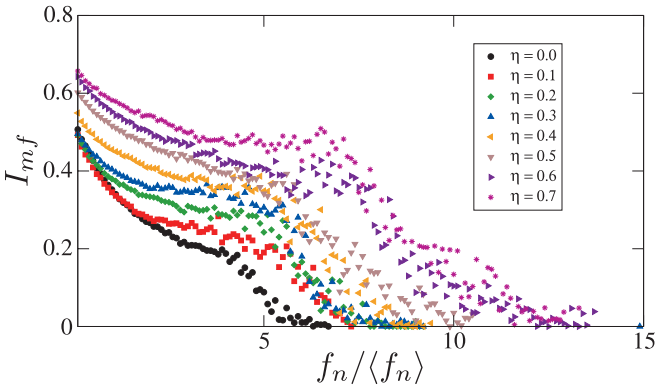

FIG. 8. (Color online) Friction mobilization I_{mf} as the average by force class, as a function of f_n for all η.

mobilized contacts. As η is increased the distribution becomes more uniform, and at even larger η a class of highly mobilized contacts (with I_m close to 1) appears, whereas the distribution is nearly uniform for all other contacts. This class belongs to weak force network, as was shown previously, so that not only the friction mobilization I_m but also the number of highly mobilized contacts are larger in the weak force network. A class of very weak forces was also evidenced in Ref. [41] in a packing of disks deposited under gravity and tilted toward its angle of stability. This subclass of the weak network can be defined as the class of contacts where the normal force is below the mean but the friction is highly or fully mobilized.

This enhanced friction mobilization implies that the equilibration of the particles is more complex than in disk packings. In particular, the nematic ordering due to the "geometrical" chains of side-side contacts between particles means that the statistics of forces and the mobilization of friction are closely related to the equilibrium of such chains rather than that of individual particles. These chains are evidenced in Fig. 10 for $\eta = 0.7$ where the force-bearing particles belonging to the chains are represented by a color level proportionally to their orientations. The friction needs to be highly mobilized inside the chains in order to ensure their stability.

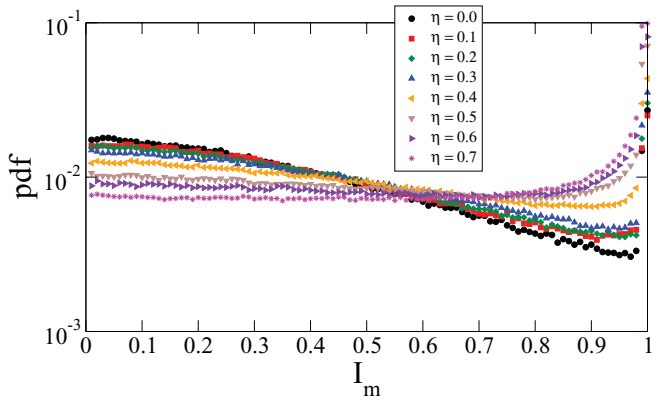

FIG. 9. (Color online) Probability distribution function of the friction mobilization index I_m.

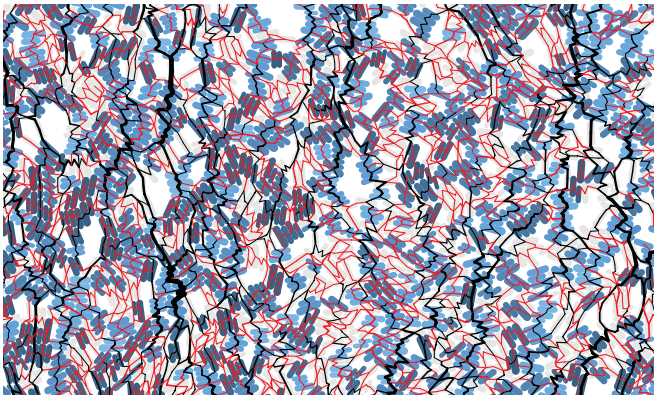

FIG. 10. (Color online) A snapshot of the force-bearing particles at $\eta = 0.7$ and normal forces represented by the thickness of the segments joining the particle centers to the application point of the force. The color level for the particles is proportional to the orientation of the major particle axis for the particles with at least one side-side contact. The particles having no side-side contacts are in gray. The strong and weak forces are in black and red (dark gray), respectively.

B. Branch vectors

The branch vectors in a packing of elongated particles reflect both the relative orientations of the particles in contact and their size distribution. The latter may be integrated out by simply dividing the branch vector length ℓ between two touching particles by the sum $R_1 + R_2$ of the radii R_1 and R_2 of their circumscribing circles. This *reduced* branch-vector length $\ell_r = \ell/(R_1 + R_2)$ varies in the range $[1 - \eta, 1]$. We have $\ell_r = 1$ at $\eta = 0$ (for disks). For elongated particles, $\ell_r = 1$ corresponds to a cap-cap contact between two aligned particles, Fig. 11(a), whereas $\ell_r = 1 - \eta$ corresponds to a centered side-side contact between two parallel particles, Fig. 11(b). Such contact configurations, when they exist, can be evidenced from the probability density function of ℓ_r and its possible modes at $\ell_r = 1$ or $\ell_r = 1 - \eta$.

Figure 12 displays the PDF of reduced branch-vector lengths for all values of η in the critical state. These PDFs are nothing but normalized radial functions with ℓ_r varying in a limited range as only the touching particles are considered. They are similar for all values of η. The first mode, centered on $\ell_r = 1 - \eta$, reveals the presence of a broad population of side-side contacts with a peak increasing in amplitude with η as displayed in Fig. 13(b). We also observe a less pronounced mode, centered on $\ell_r \simeq 1$, corresponding to a distinct population of aligned cap-cap contacts, also marked in Fig. 13(a). The intermediate mode occurs approximately at $\ell_r \simeq 1 - \eta/2$, which is the midpoint of the interval $[1 - \eta, 1]$. This length corresponds to an orthogonal side-cap contact as shown in Fig. 11(c). The presence of such a distinct mode, through decreasing in amplitude as η increases, is a clear proof of the occurrence of orthogonal layers, some of which

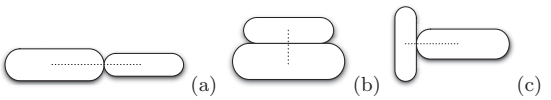

FIG. 11. Principal contact modes: cap-cap (a), side-side (b), and cap-side (c).

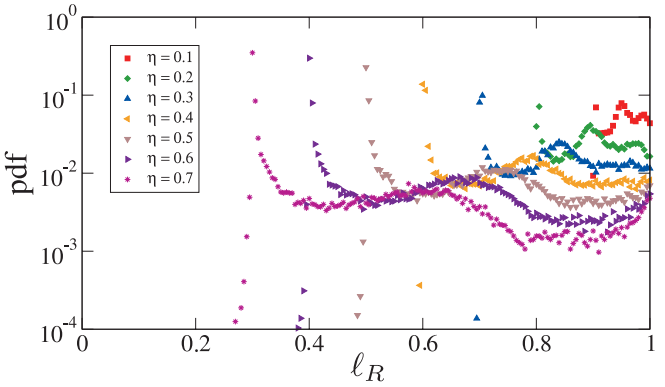

FIG. 12. (Color online) Probability distribution function of the reduced branch-vector lengths ℓ_r for all values of η in the critical state.

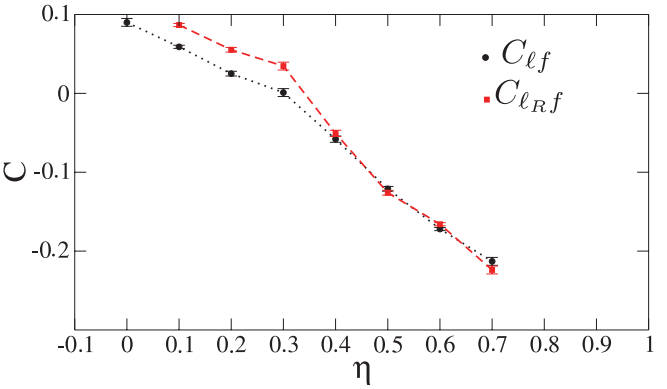

FIG. 14. (Color online) Correlation $C_{\ell_R f}$ and $C_{\ell f}$ as a function of η averaged in the critical state.

are observed in Fig. 13. This mode is also characterized by a broad extension reflecting the intermediate angles between the orientations of touching particles.

We expect the branch vector lengths to be correlated with contact forces because of either the contact configurations they represent or simply the fact that force chains tend to be captured by larger particles (hence, longer branch vectors) [12]. This correlation can be estimated with the Pearson coefficient, which for two random variables x and y is defined by the scalar

$$C_{xy} = \frac{\langle (x - \langle x \rangle)(y - \langle y \rangle) \rangle}{\sqrt{\langle (x - \langle x \rangle)^2 \rangle} \sqrt{\langle (y - \langle y \rangle)^2 \rangle}}, \tag{8}$$

Note that $C = 1$ corresponds to a full interdependence whereas $C = 0$ means full statistical independence of the two variables. Figure 14 shows the Pearson coefficients $C_{f\ell_r}$, between the force amplitude f and ℓ_r, as well as $C_{f\ell}$, between f and ℓ, as a function of η. Both coefficients decrease with η from positive values for $\eta \leqslant 0.3$ to negative values down to -0.22. The positive correlation (larger forces at longer branch vectors) is a consequence of the fact that the distribution of branch lengths at low values of η is governed by particle sizes. On the other hand, the negative correlation (larger forces at shorter branch vectors) reflects the effect of the increasing number of side-side contacts as the particles become more elongated.

Further insight into this force and branch-length correlation can be obtained from the average force amplitude $\langle f \rangle_{\ell_r}$, calculated by taking the average force in a class of contacts in the interval $[\ell_r - \Delta\ell_r/2, \ell_r + \Delta\ell_r/2]$, as a function of ℓ_r, shown in Fig. 15(a) for all values of η. This plot shows that for all contact classes the associated mean force $\langle f \rangle_{\ell_r}$ is nearly equal to the global mean force $\langle f \rangle$ except to the class of the shortest branch vectors (side-side mode), which

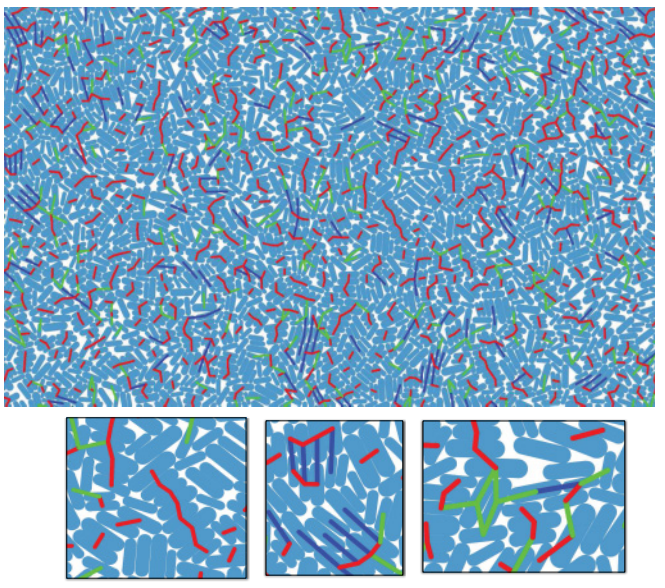

FIG. 13. (Color online) A snapshot of cap-cap modes contact (blue [black]), side-side modes contacts (red [dark gray]), and cap-side modes contacts (green [light gray]).

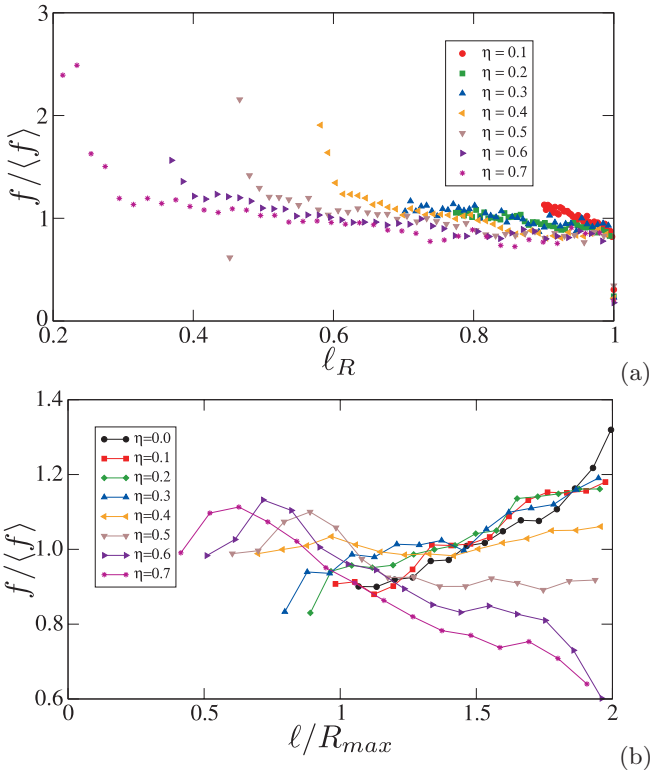

FIG. 15. (Color online) Linear correlation between contact force f and branch length ℓ as a function of η.

concentrates a mean force above $\langle f \rangle$, and the class of the longest branch vectors (cap-cap mode), which seem to carry a considerably lower force on the average. In his way, the rather weak correlation between the reduced branch length and force appears here to be governed by the two aforementioned modes. In order to evidence the effect of particle size distribution, let us consider the average force amplitude $\langle f \rangle_\ell$ as a function of ℓ as shown in Fig. 15(b) for all values of η. For $\eta \leqslant 0.3$, the contact force is on the average an increasing function of ℓ. For disks ($\eta = 0$), the variation of ℓ is a consequence only of the particle size distribution and, therefore, the increase of the mean force with ℓ means that the larger particles, involved in the longer branch vectors, capture higher forces. The same effect seems thus to underly also the increasing mean force with η for elongated particles with $\eta \leqslant 0.3$. But at larger elongations, the trend is reversed, and we see that the mean force declines as ℓ increases, reflecting thus the effect of the side-side contact mode as discussed previously.

IV. WEAK AND STRONG FORCE NETWORKS

The complex network of contact forces in a packing of elongated particles can also be analyzed by considering the contribution of various classes of forces and/or branch vectors to stress transmission. Indeed, according to Eq. (2), the stress tensor is expressed as an average involving branch vectors and contact forces, so that partial summations allow one to define partial stress tensors that have been applied in the past to investigate the scale-up of local quanties [11]. For example, the subset of contacts carrying a force below a threshold reveals the respective roles of weak and strong force chains with respect to the overall shear strength of granular materials [11]. In this section, we apply this methodology to analyze the stress and other texture-dependent quantities in view of elucidating the effect of particle elongation.

In what follows, we consider various fabric and force parameters for the "ξ networks" defined as the subsets $\mathcal{S}(\xi)$ of contacts which carry a force below a cutoff force ξ normalized by the mean force (i.e., $f_n/\langle f_n \rangle \in [0,\xi]$), where ξ is varied from 0 to the maximal force in the system. The *weak* network corresponds to $\mathcal{S}(1)$ whereas the *strong* network is its complement. In Sec. III, we focused on scalar descriptors of granular texture such as the distributions and correlations of force magnitudes and branch lengths. Beyond these low-order quantities, the granular texture is characterized by a disordered but anisotropic structure of both the contact and force networks, which require higher-order description in terms of various fabric and force tensors. We analyze below different parameters pertaining to this tensorial organization of our packings as a function of ξ and for increasing elongation η.

A. Granular texture

A relevant description of granular texture is given by the probability distribution $P(\boldsymbol{n})$ of the contact normals $\boldsymbol{n}$; see Fig. 3. In two dimensions, the unit vector $\boldsymbol{n}$ is described by a single angle $\theta \in [0,\pi]$. The distribution $P_\theta(\theta)$ of contact orientations can be evaluated from the numerical data at different stages of its evolution. In our simulations, all numerical samples are prepared in an isotropic state so that $P_\theta = 1/\pi$ in the initial state. This distribution evolves with shear strain and becomes increasingly more anisotropic as the critical state is approached. By restricting the data to those belonging to the ξ networks, we obtain a continuous family of distributions $P_\theta(\theta,\xi)$ that describe the geometrical state of the system. In practice, however, such functions can be estimated with meaningful statistics only in the critical state where the data can be cumulated from independent configurations representing all the same state.

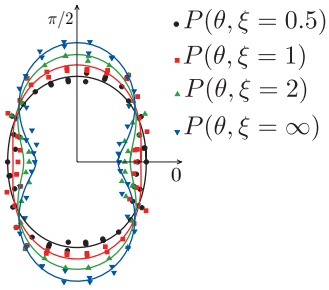

FIG. 16. (Color online) Distributions of contact orientations (symbols) in polar coordinates for $\eta = 0.5$ and several values of the force cutoff ξ together with their Fourier fits (11) (full lines).

Figure 16 shows the distributions $P_\theta(\theta,\xi)$ in polar coordinates for $\eta = 0.5$ and for several values of ξ. The distributions are similar with nearly the same privileged direction aligned with the principal stress direction $\theta_\sigma = \pi/2$ but with increasing anisotropy as a function of ξ. They all can be approximated by their truncated Fourier expansion [11,13,15]:

$$P_\theta(\theta,\xi) = \frac{1}{\pi}\{1 + a_c(\xi)\cos 2(\theta - \theta_\sigma)\}, \tag{9}$$

where $a_c(\xi)$ is the amplitude of contact anisotropy in the ξ network. In practice, it is more convenient to estimate $a_c(\xi)$ through the partial fabric tensors $\boldsymbol{F}(\xi)$ defined by [42]:

$$F_{\alpha\beta}(\xi) = \int_0^\pi n_\alpha(\theta) n_\beta(\theta) P_\theta(\theta,\xi) d\theta, \tag{10}$$

where α and β design the Cartesian components. By definition, we have $\mathrm{tr}(\boldsymbol{F}(\xi)) = 1$. Introducing the harmonic expression (9) in (10), we get

$$a_c(\xi) = 2(F_1(\xi) - F_2(\xi))\cos 2[\theta_c(\xi) - \theta_\sigma], \tag{11}$$

where the subscripts 1 and 2 refer to the principal values of $\boldsymbol{F}(\xi)$ and $\theta_c(\xi)$ represents the privileged direction of the partial fabric tensors $\boldsymbol{F}(\xi)$. Note that, up to statistical fluctuations, the principal directions of the fabric and stress tensors coincide in the critical state for each ξ network, so that the phase factor $\cos 2[\theta_c(\xi) - \theta_\sigma]$ is either equal to 1 when $\theta_c(\xi) = \theta_\sigma$ or equal to -1 when $\theta_c(\xi) = \theta_\sigma + \pi/2$.

Figure 17 displays a_c as a function of ξ for all values of η. For the disk packings ($\eta = 0$), the anisotropy of weak contacts is negative but increases in absolute value and reaches its peak value at $\xi \sim 1$. This negative value indicates that in disk packings the weak contacts are orientated preferentially perpendicular to the major principal stress direction [11]. As more contacts come into play with increasing ξ, the partial anisotropy $a_c(\xi)$ becomes less negative and finally changes sign, showing that the strong contacts are mainly along the

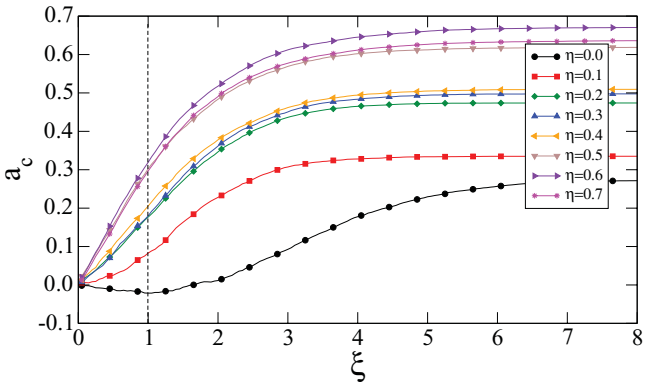

FIG. 17. (Color online) Partial fabric anisotropy a_c as a function of force cutoff ξ normalized by the mean force $\langle f \rangle$ for different values of η.

major principal stress direction. This bimodal behavior of stress transmission is a nontrivial organization of the force network and holds also in three dimensions (3D), in the case of sphere packings [16]. However, it is remarkable that for elongated particles ($\eta > 0$), the partial anisotropies of both weak and strong networks are positive, as observed in Fig. 17. This means that, in contrast to the disk packings, the weak and strong contacts in packings of elongated particles cannot be differentiated on the basis of their roles in the ξ networks. Physically, this behavior may be interpreted by stating that the static equilibrium of the chains of elongated particles does not require the stabilizing effect of the weak contacts. A similar result was observed by Estrada *et al.* for disk packings at large values of rolling resistance, which allows for the equilibrium of long chains of particles interconnected by only two contacts [13]. But, as we see below, for our elongated particles the differentiation between the two networks operates via the forces carried by the ξ networks.

The information involved in the angular distribution P_θ may be enriched by accounting for the branch vectors $\boldsymbol{\ell}$ which, as seen in Sec. III, reflects both the particle size distribution and local contact modes. We thus consider here the average normal and tangential branch vector components $\langle \ell_n \rangle(\theta,\xi)$ and $\langle \ell_t \rangle(\theta,\xi)$ defined in Eq. (4), obtained by averaging ℓ_n and ℓ_t over the contacts oriented along θ within a centered angular interval $\Delta\theta$. As for P_θ, we evaluate these functions in the critical state, for different values of η and as ξ. Figure 18 shows the functions $\langle \ell_n \rangle(\theta,\xi)$ and $\langle \ell_t \rangle(\theta,\xi)$ in polar coordinates for $\eta = 0.5$ and for several values of ξ. These functions are anisotropic with an anisotropy which depends on ξ. We introduce here their truncated expansion on an orthonormal Fourier basis:

$$\begin{aligned} \langle \ell_n \rangle(\theta,\xi) &= \langle \ell_n \rangle(\xi)\{1 + a_{ln}(\xi)\cos 2(\theta - \theta_\sigma)\}, \\ \langle \ell_t \rangle(\theta,\xi) &= \langle \ell_n \rangle(\xi) a_{lt}(\xi)\sin 2(\theta - \theta_\sigma), \end{aligned} \tag{12}$$

where $a_{ln}(\xi)$ and $a_{lt}(\xi)$ are the normal and tangential branch anisotropies in the ξ networks. Note that by construction we have $a_{lt} = 0$ for disks ($\eta = 0$). The analytical form of $\langle \ell_t \rangle(\theta,\xi)$ results from the orthonormal nature of the Fourier basis and the fact that the mean value of ℓ_t vanishes due to axial symmetry:

$$\int_0^\pi \langle \ell_t \rangle(\theta,\xi)\, P_\theta(\theta,\xi)\, d\theta = 0. \tag{13}$$

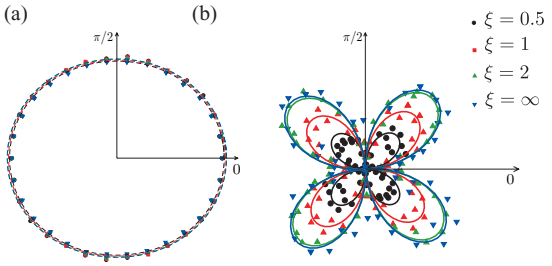

FIG. 18. (Color online) Distributions of $\langle \ell_n \rangle(\theta,\xi)$ (a) and $\langle \ell_t \rangle(\theta,\xi)$ (b) (symbols) in polar coordinates for $\eta = 0.5$ and several values of the force cutoff ξ together with their Fourier fits (19) (full lines). Note that the amplitudes are always negative for $\langle \ell_t \rangle(\theta,\xi)$ as shown in Fig. 19.

Figure 18 shows that this functional form provides a good approximation of the data.

For the calculation of $a_{ln}(\xi)$ and $a_{lt}(\xi)$, we introduce the following *branch tensors* [18]:

$$\begin{aligned} \chi^{ln}_{\alpha\beta}(\xi) &= \int_0^\pi \langle \ell_n \rangle(\theta,\xi) n_\alpha(\theta) n_\beta(\theta) P_\theta(\theta,\xi) d\theta, \\ \chi^{lt}_{\alpha\beta}(\xi) &= \int_0^\pi \langle \ell_t \rangle(\theta,\xi) n_\alpha(\theta) t_\beta(\theta) P_\theta(\theta,\xi) d\theta, \end{aligned} \tag{14}$$

The following relations are then easily obtained:

$$\begin{aligned} a_{ln}(\xi) &= 2\frac{\chi^{ln}_1(\xi) - \chi^{ln}_2(\xi)}{\mathrm{tr}[\boldsymbol{\chi}^{ln}(\infty)]} - a_c(\xi), \\ a_{lt}(\xi) &= 2\frac{\chi^{l}_1(\xi) - \chi^{l}_2(\xi)}{\mathrm{tr}[\boldsymbol{\chi}^{l}(\infty)]} - a_c(\xi) - a_{ln}(\xi), \end{aligned} \tag{15}$$

where $\boldsymbol{\chi}^l = \boldsymbol{\chi}^{ln} + \boldsymbol{\chi}^{lt}$ and the subscripts 1 and 2 refer to the principal values of each tensor. By construction, we have $\mathrm{tr}\boldsymbol{\chi}^l = (\chi^l_1 + \chi^l_2) = \langle \ell_n \rangle$. Note also that the two partial branch vector anisotropies a_{ln} and a_{lt} may be positive or negative.

Figure 19 shows the branch-vector anisotropies $a_{ln}(\xi)$ and $a_{lt}(\xi)$ as a function of ξ in the critical state for all values of η. $a_{ln}(\xi)$ is positive for $\eta = 0$ and $\eta = 0.1$ and increases slightly with ξ, but for more elongated particles it takes negative values, which means that the particles tend to form longer branch vectors with their neighbors in the direction of extension. As ξ increases, this anisotropy increases in absolute value and reaches a plateau after passing by a peak value at a point in the range $\xi \in [1,2]$. This behavior suggests that the particles touch preferentially along their minor axes when the contact orientation is close to the compression axis (in the strong network) and along their major axis when the contact orientation is close to the extension axis (in the weak network), in agreement with the fact that the longest branches are in the weak network; see Sec. III. As for $a_{lt}(\xi)$, its value is always negative and increases monotonically with ξ in absolute value. Note also that, for all values of ξ, $a_{lt}(\xi)$ is much higher than $a_{ln}(\xi)$, while both remain weak compared to $a_c(\xi)$.

B. Force anisotropies

We now consider the angle-averaged normal and tangential forces, $\langle f_n \rangle(\theta,\xi)$ and $\langle f_t \rangle(\theta,\xi)$, in the ξ network. A second-order Fourier expansion provides an adequate representation

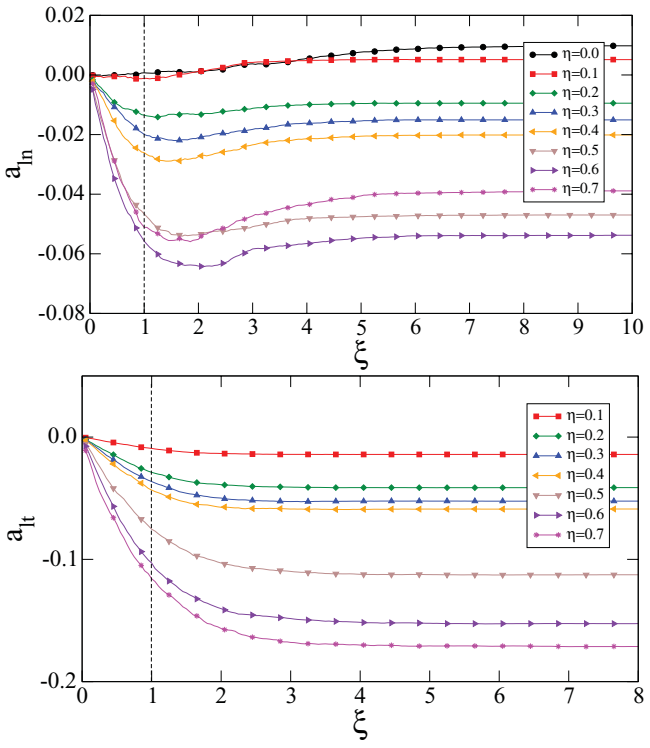

FIG. 19. (Color online) Partial normal and tangential branch vector length anisotropies a_{ln} and a_{lt} as a function of force cutoff ξ normalized by the mean force $\langle f \rangle$ for different values of η.

of these distributions for all values of ξ as shown in Fig. 20:

$$\begin{aligned} \langle f_n \rangle(\theta,\xi) &= \langle f_n \rangle(\xi)\{1 + a_{fn}(\xi)\cos 2(\theta - \theta_\sigma)\} \\ \langle f_t \rangle(\theta,\xi) &= \langle f_n \rangle(\xi) a_{ft}(\xi)\sin 2(\theta - \theta_\sigma), \end{aligned} \tag{16}$$

where $a_{fn}(\xi)$ and $a_{ft}(\xi)$ are the amplitudes of normal and tangential force anisotropies in the ξ networks. Notice that we have $\langle f_t \rangle = 0$ as a consequence of the balance of force moments, which is also at the origin of the symmetry of the stress tensor. More generally, $\langle f_n \rangle(\theta)$ and $\langle f_t \rangle(\theta)$ behave like the components $\sigma_n(\theta) = \sigma n.n$ and $\sigma_t(\theta) = \sigma n.t$ of the stress tensor on a plane oriented along the direction θ, although they do not derive from a single tensor. This analogy works also for the peak value of $\langle f_t \rangle(\theta,\xi)$, which occurs at an angle rotated by $\pi/4$ with respect to that of $\langle f_n \rangle(\theta,\xi)$.

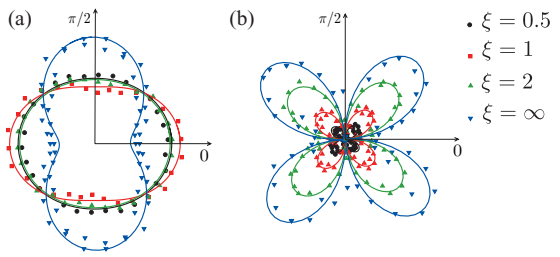

FIG. 20. (Color online) Distributions of $\langle f_n \rangle(\theta,\xi)$ (a) and $\langle f_t \rangle(\theta,\xi)$ (b) (symbols) in polar coordinates for $\eta = 0.5$ and several values of the force cutoff ξ together with their Fourier fits (16) (full lines). Note that the amplitudes are always positive for $\langle f_t \rangle(\theta,\xi)$ as shown in Fig. 21.

As for the branch length vectors, the calculation of the anisotropy parameters $a_{fn}(\xi)$ and $a_{ft}(\xi)$ can be done by means of the following *force tensors* [11,18]:

$$\begin{aligned} \chi^{fn}_{\alpha\beta}(\xi) &= \int_0^\pi \langle f_n \rangle(\theta,\xi) n_\alpha(\theta) n_\beta(\theta) P_\theta(\theta,\xi) d\theta, \\ \chi^{ft}_{\alpha\beta}(\xi) &= \int_0^\pi \langle f_t \rangle(\theta,\xi) n_\alpha(\theta) t_\beta(\theta) P_\theta(\theta,\xi) d\theta. \end{aligned} \tag{17}$$

With these definitions, the following relationships can easily be established:

$$a_{fn}(\xi) = 2\frac{\chi_1^{fn}(\xi) - \chi_2^{fn}(\xi)}{\mathrm{tr}[\boldsymbol{\chi}^{fn}(\infty)]} - a_c(\xi), \tag{18}$$

$$a_{ft}(\xi) = 2\frac{\chi_1^{f}(\xi) - \chi_2^{f}(\xi)}{\mathrm{tr}[\boldsymbol{\chi}^{f}(\infty)]} - a_c(\xi) - a_{fn}(\xi), \tag{19}$$

where $\boldsymbol{\chi}^f = \boldsymbol{\chi}^{fn} + \boldsymbol{\chi}^{ft}$ and the indices 1 and 2 refer to the principal values of each tensor. By construction, we have $\mathrm{tr}(\boldsymbol{\chi}^f) = \chi_1^f + \chi_2^f = \langle f_n \rangle$. The two partial force anisotropies a_{fn} and a_{ft} may take positive or negative.

The normal and tangential force anisotropies are plotted in Fig. 21 as a function of ξ for all values of η. A remarkable feature of $a_{fn}(\xi)$ is that its value is negative in the weak network ($\xi < 1$) for all elongated particles, that is, for all values of η with the exception of $\eta = 0$, where it remains positive for all ξ. Hence, the weak forces in a packing of elongated particles occur at contacts preferentially oriented orthogonally to the principal stress direction θ_σ whereas in a disk packing they are parallel. As we saw before, an inverse

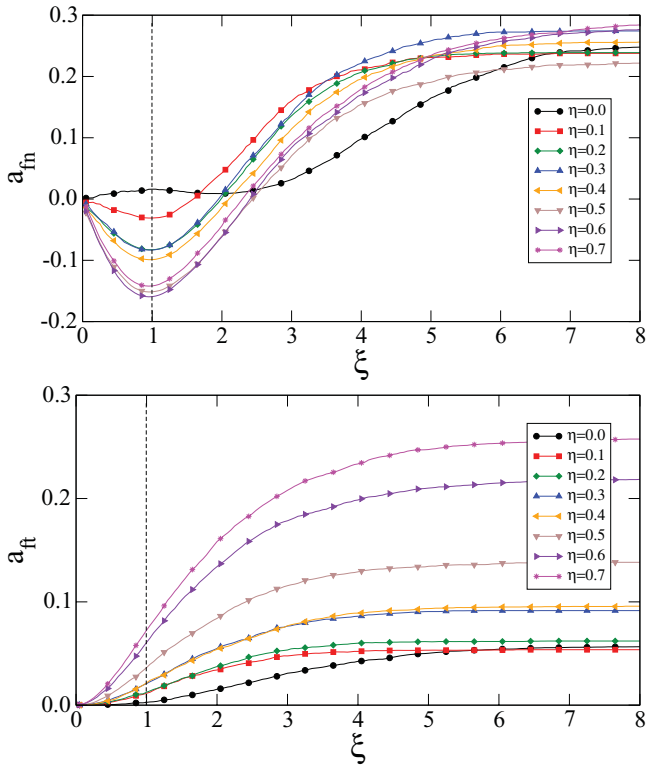

FIG. 21. (Color online) Partial normal and tangential force anisotropies a_{fn} and a_{ft} as functions of force cutoff ξ normalized by the mean force $\langle f \rangle$ for different values of η.

behavior occurs for the contact anisotropies; that is, the weak contacts in the packings of elongated particles are parallel to the principal stress direction and orthogonal for the disk packings. $a_{fn}(\xi)$ increases in absolute value as ξ increases and passes by a peak at exactly $\xi = 1$, then declines as more contacts from the strong network with a positive contribution to the anisotropy are included in the ξ network. At larger values (beyond $\xi \simeq 2$ for nearly all values of η), $a_{fn}(\xi)$ becomes positive as the strong forces tend to be parallel to the principal stress direction. This unmonotonic behavior of the partial force anisotropies for the elongated particles and the partial contact anisotropies for the disk packings underlies the differentiation between the weak and strong networks according to the values of the normal contact forces with respect to the mean force ($\xi = 1$). The difference between the elongated particle packings and disk packings reflects the formation of side-side contacts oriented along the principal stress direction tending to capture the strong force chains.

The tangential force anisotropy $a_{ft}(\xi)$ is an increasing function of both ξ and η. Its value is generally below $a_{fn}(\xi)$ but becomes comparable for the most elongated particles for which the friction mobilization plays a key role, as discussed previously. This is plausible as the tangential force anisotropy represents friction mobilization at contacts oriented at $\pi/4$ with respect to the major principal stress direction.

C. Stress tensor

The physical importance of geometrical and mechanical anisotropies becomes clear when it is considered in connection with the stress tensor. As shown by Eq. (2), the stress tensor is a function of discrete microscopic parameters attached to the contact network. It is also possible to attribute a stress tensor to each ξ network by restricting the summation to the corresponding contacts:

$$\boldsymbol{\sigma}(\xi) = \frac{1}{V} \sum_{c \in V} f_\alpha^c(\xi) \ell_\beta^c(\xi). \tag{20}$$

For sufficiently large systems, the dependence of volume averages on individual discrete parameters vanishes [18,43] and the discrete sums can be replaced by integrals as follows:

$$\sigma_{\alpha\beta}(\xi) = n_c \int_\Omega f_\alpha(\xi) \ell_\beta(\xi)\ P_\xi(\boldsymbol{\ell f}) d\boldsymbol{f}\ d\boldsymbol{\ell}, \tag{21}$$

where $P_\xi(\boldsymbol{\ell f})$ is the joint probability density of forces and branch vectors in the ξ networks, n_c is the number density of contacts for the whole system, and Ω is the integration domain in the space $(\boldsymbol{\ell}, \boldsymbol{f})$.

The integral appearing in Eq. (21) can be reduced by integrating first with respect to the forces and branch vector lengths. Considering the components of the forces and branch vectors in contact frames $(\boldsymbol{n}, \boldsymbol{t})$, and assuming that branch-force correlations can be neglected in each ξ network as in the whole network (see Fig. 14), we get [16,18,43]

$$\begin{aligned}\sigma_{\alpha\beta}(\xi) = n_c \int_0^\pi \{&\langle \ell_n \rangle(\theta,\xi)\ n_\alpha(\theta) \\ &+ \langle \ell_t \rangle(\theta)\ t_\beta(\theta)\}\{\langle f_n \rangle(\theta,\xi) n_\alpha(\theta) \\ &+ \langle f_t \rangle(\theta,\xi)\ t_\beta(\theta)\} P(\theta,\xi)\ d\theta.\end{aligned} \tag{22}$$

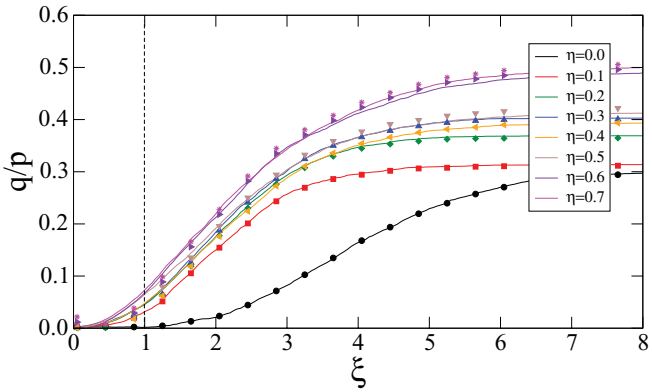

FIG. 22. (Color online) Partial shear stress q/p as a function of force cutoff ξ for different values of η (plain line) together with approximation given by Eq. (23) (points).

The expression of the stress tensor by this equation makes the average directional functions representing the fabric and force states appear explicitly.

Using the harmonic approximation introduced before, Eq. (22) can be integrated with respect to space direction θ and we get the following simple relation:

$$\frac{q(\xi)}{p} \simeq \frac{1}{2}\{a_c(\xi) + a_{ln}(\xi) + a_{lt}(\xi) + a_{fn}(\xi) + a_{ft}(\xi)\}, \tag{23}$$

where the cross products among the anisotropy parameters have been neglected. This relation expresses the normalized shear stress as a half-sum of texture and force anisotropies. Figure 22 displays the partial shear stress $q(\xi)/p$ as a function of ξ together with the approximation given by Eq. (23). As we see, Eq. (23) provides an excellent fit to the data for all values of ξ and η. Interestingly, $q(\xi < 1)/p$ is zero for disk packings, implying that strong forces carry the whole deviatoric load. The partial stress deviator $q(\xi = 1)/p$ in the weak network increases slightly with η but remains in all cases weak (below 0.1). This transition reflects a qualitative change in the condition of local force balance in the presence of clusters as shown in Fig. 10. In other words, for these packings the weak network sustains also partially the deviatoric load applied to the system. The weak values of q/p in the weak network is a consequence of the large positive value $a_c(\xi = 1) = 0.3$, which compensates the negative values of $a_{fn}(\xi = 1)$, $a_{ln}(\xi = 1)$ and $a_{lt}(\xi = 1)$.

V. SUMMARY

In summary, using contacts dynamics simulations, we analyzed the granular texture and topology of forces chains in various packings composed of elongated particles under biaxial compression. As compared to disk packings, the effect of particle elongation is to enhance the heterogeneity of the packings by the clustering of the particles according to their contact modes. In particular, the side-side contacts tend to capture strong force chains and be oriented orthogonally to the major principal stress direction. These features are reinforced as the particle elongation is increased. The probability densities of the normal forces become broader with stronger force

chains characterized by an exponential distribution as in disks packings and with higher number of weak forces decreasing as a power law with the force.

An interesting finding of this work concerns the differentiation between the strong and weak force networks for elongated particles. In contrast to disks packings, where the contacts in the weak network are on average perpendicular to the contacts in the strong network, the contacts in a packing of elongated particles are, on average, oriented along the major principal stress direction both in the weak and strong networks. However, the weak forces in the case of elongated particles show a negative anisotropy in the sense that the average normal force in the weak network has its maximum value in the contacts perpendicular to the strong network. In other words, while in the disk packings the strong forces chains are propped by many weak lateral contact, for elongated particles the strong force chains are laterally sustained by less contact but larger weak forces. A harmonic decomposition of the stress tensor shows, however, that for both disks and elongated particles, the compensating effects of force and contact anisotropies lead to small shear stress deviator carried by the weak network.

Our simulation data indicate that the larger global shear strength of a packing of elongated particles increases with elongation mainly due to the increase of friction mobilization and friction force anisotropy. The normal force anisotropy is large but nearly independent of elongation. On the other hand, the correlation between contact forces and branch vectors joining particle centers reveal a subnetwork of weak contacts with high friction mobilization and small branch vector length.

In conclusion, the packings of elongated particles in 2D reveal a nontrivial texture allying the geometry of the particles with the preferred orientations of the contacts induced by shearing and equilibrium of particles. Some features are reminiscent of disk packings but are strongly modulated by the particle shape. More work is under way to clarify the effect of particle shape by focusing on the local structures. On the other hand, many aspects of the packings analyzed in this paper are specific to two dimensions. The side-side contacts in 3D between particles of spherocylindrical shape do not give rise to nematic ordering, and the particle rotations and forces moments play a major role in the equilibrium of such particles. This point can be analyzed only by performing 3D simulations of large packings of spherocylinders of varying elongation. However, since the class of side-side contacts controls to a large extent the specific behavior of elongated particles in 2D, we believe that similar features should occur in 3D for platy particles, which may give spontaneously rise to geometrical chains of face-face contacts. Such simulations require, however, much more computational effort.

[1] C. Liu, S. R. Nagel, D. A. Schecter, S. N. Coppersmith, S. Majumdar, O. Narayan, and T. A. Witten, Science **269**, 513 (1995).

[2] F. Radjai, M. Jean, J. J. Moreau, and S. Roux, Phys. Rev. Lett. **77**, 274 (1996).

[3] H. M. Jaeger, S. R. Nagel, and R. P. Behringer, Rev. Mod. Phys. **68**, 1259 (1996).

[4] D. M. Mueth, H. M. Jaeger, and S. R. Nagel, Phys. Rev. E **57**, 3164 (1998).

[5] G. Lovoll, K. J. Maloy, and E. G. Flekkoy, Phys. Rev. E **60**, 5872 (1999).

[6] S. G. Bardenhagen, J. U. Brackbill, and D. L. Sulsky, Phys. Rev. E **62**, 3882 (2000).

[7] L. E. Silbert, G. S. Grest, and J. W. Landry, Phys. Rev. E **66**, 061303 (2002).

[8] L. E. Silbert, Phys. Rev. E **74**, 051303 (2006).

[9] A. R. T. van Eerd, W. G. Ellenbroek, M. van Hecke, J. H. Snoeijer, and T. J. H. Vlugt, Phys. Rev. E **75**, 060302(R) (2007).

[10] V. Richefeu, E. Azéma, F. Radjai, and S. Youssoufi, Powder Technol. **190**, 258 (2009).

[11] F. Radjai, D. E. Wolf, M. Jean, and J. J. Moreau, Phys. Rev. Lett. **80**, 61 (1998).

[12] C. Voivret, F. Radjai, J.-Y. Delenne, and M. S. El Youssoufi, Phys. Rev. Lett. **102**, 178001 (2009).

[13] N. Estrada, A. Taboada, and F. Radjai, Phys. Rev. E **78**, 021301 (2008).

[14] A. Mirghasemi, L. Rothenburg, and E. Maryas, Geotechnique **52**, 209 (2002).

[15] E. Azéma, F. Radjai, R. Peyroux, and G. Saussine, Phys. Rev. E **76**, 011301 (2007).

[16] E. Azéma, F. Radjai, and G. Saussine, Mech. Mater. **41**, 721 (2009).

[17] N. Estrada, E. Azema, F. Radjai, and A. Taboada, Phys. Rev. E **84**, 011306 (2011).

[18] E. Azéma and F. Radjaï, Phys. Rev. E **81**, 051304 (2010).

[19] C. R. Abreu and N. M. F. W. Tavares, Powder Technol. **134**, 167 (2003).

[20] A. Donev, R. Connelly, F. H. Stillinger, and S. Torquato, Phys. Rev. E **75**, 051304 (2007).

[21] A. Wouterse, S. Williams, and A. Philipse, J. Phys. Condens. Matter **19**, 406215 (2007).

[22] B. Saint-Cyr, J.-Y. Delenne, C. Voivret, F. Radjai, and P. Sornay, Phys. Rev. E **84**, 041302 (2011).

[23] I. Zuriguel, T. Mullin, and J. M. Rotter, Phys. Rev. Lett. **98**, 028001 (2007).

[24] R. C. Hidalgo, I. Zuriguel, D. Maza, and I. Pagonabarraga, Phys. Rev. Lett. **103**, 118001 (2009).

[25] T. Kanzaki, M. Acevedo, I. Zuriguel, I. Pagonabarraga, D. Maza, and R. Hidalgo, Eur. Phys. J. E **34**, 133 (2011).

[26] J.-J. Moreau, European J. Mech. A Solids **13**, 93 (1994).

[27] F. Radjai, *Physics of Dry Granular Media* (Kluwer Academic Publishers, Dordrecht, the Netherlands, 1997), p. 305.

[28] M. Jean, Comput. Methods Appl. Mech. Eng. **177**, 235 (1999).

[29] J-J. Moreau, in *Novel Approaches in Civil Engineering*, edited by M. Frémond and F. Maceri, Lecture Notes in Applied and Computational Mechanics Vol. 14 (Springer-Verlag, Berlin, 2004), pp. 1–46.

[30] F. Dubois and M. Jean, *Analysis and Simulation of Contact Problems*, edited by Wriggers, Peter and Nackenhorst, Udo,

Vol. 27 (Springer, Berlin/Heidelberg, 2006), pp. 375–378; [http://www.springerlink.com/content/y651154g0062550j].

[31] F. Radjaï and E. Azéma, Eur. J. Env. Civil Engineering **13**, 203 (2009).

[32] F. Radjai and F. Dubois (eds.), *Discrete Numerical Modeling of Granular Materials* (Wiley-ISTE, New York, 2011); [http://eu.wiley.com/WileyCDA/WileyTitle/productCd-1848212607.html].

[33] G. Saussine, C. Cholet, P. Gautier, F. Dubois, C. Bohatier, and J. Moreau, Comput. Methods Appl. Mech. Eng. **195**, 2841 (2006).

[34] E. Azéma, F. Radjai, R. Peyroux, F. Dubois, and G. Saussine, Phys. Rev. E **74**, 031302 (2006).

[35] E. Azéma, F. Radjai, R. Peyroux, V. Richefeu, and G. Saussine, Eur. Phys. J. E **26**, 327 (2008).

[36] I. Bratberg, F. Radjai, and A. Hansen, Phys. Rev. E **66**, 031303 (2002).

[37] A. Taboada, K. J. Chang, F. Radjai, and F. Bouchette, J. Geophys. Res. **110**, 1 (2005).

[38] C. Voivret, F. Radjai, J.-Y. Delenne, and M. S. El Youssoufi, Phys. Rev. E **76**, 021301 (2007).

[39] J. J. Moreau, in *Friction, Arching, Contact Dynamics*, edited by D. E. Wolf and P. Grassberger (World Scientific, Singapore, 1997), pp. 233–247.

[40] L. Staron and F. Radjai, Phys. Rev. E **72**, 041308 (2005).

[41] L. Staron, F. Radjai, and J. Vilotte, Eur. Phys. J. E **18**, 311 (2005).

[42] M. Satake, in *Proceedings of the IUTAM Symposium on Deformation and Failure of Granular Materials, Delft*, edited by P. A. Vermeer and H. J. Luger (A. A. Balkema, Amsterdam, 1982), pp. 63–68.

[43] L. Rothenburg and R. J. Bathurst, Geotechnique **39**, 601 (1989).